The Astrophysical Journal Letters, 931:L17 (7pp), 2022 June 1 https://doi.org/10.3847/2041-8213/ac6e6b

Solar-like Dynamos and Rotational Scaling of Cycles from Star-in-a-box Simulations

Petri J. Käpylä
Georg-August-Universität Göttingen, Institute for Astrophysics and Geophysics, Friedrich-Hund-Platz 1, D-37077 Göttingen, Germany; pkaepyl@uni-goettingen.de
Received 2022 February 9; revised 2022 May 2; accepted 2022 May 10; published 2022 May 26

Abstract

Magnetohydrodynamic star-in-a-box simulations of convection and dynamos in a solar-like star with different rotation rates are presented. These simulations produce solar-like differential rotation with a fast equator and slow poles and magnetic activity that resembles that of the Sun with equatorward migrating activity at the surface. Furthermore, the ratio of rotation to cycle period is almost constant, as the rotation period decreases in the limited sample considered here. This is reminiscent of the suggested inactive branch of stars from observations and differs from most earlier simulation results from spherical shell models. While the exact excitation mechanism of the dynamos in the current simulations is not yet clear, it is shown that it is plausible that the greater freedom that the magnetic field has due to the inclusion of the radiative core and regions exterior to the star are important in shaping the dynamo.

Unified Astronomy Thesaurus concepts: Stellar magnetic fields (1610); Magnetohydrodynamical simulations (1966); Astrophysical fluid dynamics (101)

Supporting material: animation

1. Introduction

The Sun maintains a global dynamo with a magnetic cycle of approximately 22 yr, with activity appearing at the surface at midlatitudes and propagating equatorward as the cycle progresses (e.g., Hathaway 2010). Three-dimensional magnetohydrodynamic simulations struggle to reproduce such cycles; often, the activity propagates poleward (e.g., Brown et al. 2011; Nelson et al. 2013), active latitudes do not coincide with those in the Sun (e.g., Ghizaru et al. 2010), or there is a mismatch between the simulated and solar cycle periods (e.g., Käpylä et al. 2012; Warnecke 2018). Furthermore, the simulations usually require substantially faster rotation than in the Sun to achieve cyclic dynamos (e.g., Viviani et al. 2018). Another issue arises when simulations at different rotation rates are confronted with observations; cycles observed from stars other than the Sun suggest that in the vicinity of the solar Rossby number, which is the ratio of the rotation period to convective turnover time, the ratio of rotation to cycle period increases as the Rossby number decreases (e.g., Olspert et al. 2018). Simulations often produce the opposite trend (e.g., Strugarek et al. 2018; Warnecke 2018). Typically, more than one of these defects is found in any given simulation.

There are several possible reasons for the mismatch between simulations and reality. A major factor in this is likely to be the inability of current simulations to capture stellar convective flows accurately enough. This is known as the convective conundrum and manifested by too-high large-scale velocity amplitudes in simulations in comparison to the Sun (e.g., Hanasoge et al. 2012; O'Mara et al. 2016; Schumacher & Sreenivasan 2020). This often leads to antisolar differential rotation in simulations with solar luminosity and rotation rate (e.g., Käpylä et al. 2014), and very high resolutions, in addition to highly supercritical dynamos, are likely needed to overcome this (Hotta & Kusano 2021).

Another factor is that stellar dynamo simulations are often done in spherical shells where only the convection zone (CZ) or, additionally, a part of the radiative core is modeled (e.g., Guerrero et al. 2019; Bice & Toomre 2020). This necessitates the use of boundary conditions that may not always be appropriate and can affect the dynamo solutions in ways that are a priori not obvious (e.g., Cole et al. 2016). In the present study, a star-in-a-box model, where a spherical star is embedded into a Cartesian cube, is used to model a solar-like star in a rotational regime where cyclic solutions are excited. The model thus includes the radiative core and regions exterior to the star. The former enables contributions to the dynamo from the interface between the radiative and convective zones, whereas the latter is usually not considered to be important in the maintenance of the dynamo. However, including the exterior is less restrictive than imposing mathematically or numerically convenient boundary conditions at the surface that can also affect the resulting dynamos (e.g., Warnecke et al. 2016).

2. Model

The star-in-a-box model described in Käpylä (2021) is used; see also Dobler et al. (2006). A star of radius R is embedded into a Cartesian cube with side length $H = 2.2R$. The governing equations are

$$\frac{\partial \boldsymbol{A}}{\partial t} = \boldsymbol{U} \times \boldsymbol{B} - \eta\mu_0 \boldsymbol{J}, \tag{1}$$

$$\frac{D \ln \rho}{Dt} = -\boldsymbol{\nabla} \cdot \boldsymbol{U}, \tag{2}$$

$$\frac{D\boldsymbol{u}}{Dt} = -\boldsymbol{\nabla}\Phi - \frac{1}{\rho}(\boldsymbol{\nabla} p - \boldsymbol{\nabla} \cdot 2\nu\rho\mathbf{S} - \boldsymbol{J} \times \boldsymbol{B}) - 2\boldsymbol{\Omega} \times \boldsymbol{U} + \boldsymbol{f}_d, \tag{3}$$

$$\rho T\frac{Ds}{Dt} = -\boldsymbol{\nabla}\cdot(\boldsymbol{F}_{\rm rad}+\boldsymbol{F}_{\rm SGS}) + \mathscr{H} - \mathscr{C} + 2\nu\mathsf{S}^2 + \mu_0\eta\boldsymbol{J}^2, \quad (4)$$

where $\boldsymbol{A}$ is the magnetic vector potential, $\boldsymbol{U}$ is the velocity, $\boldsymbol{B}=\boldsymbol{\nabla}\times\boldsymbol{A}$ is the magnetic field, $\boldsymbol{J}=\boldsymbol{\nabla}\times\boldsymbol{B}/\mu_0$ is the current density, μ_0 is the permeability of vacuum, η is the magnetic diffusivity, $D/Dt=\partial/\partial t+\boldsymbol{U}\cdot\boldsymbol{\nabla}$ is the advective derivative, ρ is the fluid density, Φ is the gravitational potential, p is the pressure, and ν is the kinematic viscosity. The traceless rate-of-strain tensor is given by $\mathsf{S}_{ij}=\frac{1}{2}\left(\frac{\partial U_i}{\partial x_j}+\frac{\partial U_j}{\partial x_i}\right)-\frac{1}{3}\delta_{ij}\boldsymbol{\nabla}\cdot\boldsymbol{U}$, where δ_{ij} is the Kronecker delta. The angular velocity is given by $\boldsymbol{\Omega}=(0,\ 0,\ \Omega_0)$, f_d is a damping function, T is the temperature, and s is the specific entropy. The $\boldsymbol{F}_{\rm rad}$ and $\boldsymbol{F}_{\rm SGS}$ are the radiative and subgrid-scale (SGS) entropy fluxes, and $\mathscr{H}$ and $\mathscr{C}$ describe heating and cooling, respectively.

An ideal gas equation of state with $p=\mathcal{R}\rho T$ is used, where $\mathcal{R}=c_{\rm P}-c_{\rm V}$ is the gas constant, and $c_{\rm P}$ and $c_{\rm V}$ are the heat capacities at constant pressure and volume, respectively. The gravitational potential Φ corresponds to an isentropic polytrope of a main-sequence M5 star (see Appendix A of Dobler et al. 2006). Flows in the exterior to the star are damped through the term $\boldsymbol{f}_d=-\frac{\boldsymbol{U}}{\tau_{\rm damp}}f_{\rm e}(r)$, where $\tau_{\rm damp}$ is a damping timescale, and $f_{\rm e}(r)=\frac{1}{2}\left(1+\tanh\frac{r-r_{\rm damp}}{w_{\rm damp}}\right)$, where $r_{\rm damp}=1.03R$, and $w_{\rm damp}=0.03R$. The damping timescale $\tau_{\rm damp}\approx 0.2\tau_{\rm ff}$, where $\tau_{\rm ff}=\sqrt{R^3/GM}$ is the freefall time, G is the gravitational constant, and M is the mass of the star.

The radiative flux is given by $\boldsymbol{F}_{\rm rad}=-K\boldsymbol{\nabla}T$, where

$$K(\rho,\ T)=K_0(\rho/\rho_0)^{a-1}(T/T_0)^{b+3}, \quad (5)$$

where $a=-1$ and $b=7/2$ correspond to the Kramers opacity law (e.g., Brandenburg et al. 2000). Additional SGS entropy flux is included with $\boldsymbol{F}_{\rm SGS}=-\chi_{\rm SGS}\rho\boldsymbol{\nabla}s'$, where $s'=s-\langle s\rangle_t$ is the fluctuation of the entropy, and $\langle s\rangle_t(\boldsymbol{x},\ t)$ is a running temporal mean computed over an interval of 10 freefall times. Nuclear energy production in the core of the star is parameterized by the heating term $\mathscr{H}$ with a Gaussian profile, $\mathscr{H}(r)=\frac{L_{\rm sim}}{(2\pi w_L^2)^{3/2}}\exp\left(-\frac{r^2}{2w_L^2}\right)$, where $L_{\rm sim}$ is the luminosity, and $w_L=0.162R$ is the width of the Gaussian. The cooling term $\mathscr{C}$ models radiative losses above the stellar surface with $\mathscr{C}(\boldsymbol{x})=\rho c_{\rm P}\frac{T(\boldsymbol{x})-T_{\rm surf}}{\tau_{\rm cool}}f_{\rm e}(r)$, where $\tau_{\rm cool}=\tau_{\rm damp}$ is a cooling timescale, and $T_{\rm surf}$ is the fixed surface temperature.

The fluid and magnetic Reynolds numbers and the Péclet number are given by ${\rm Re}=u_{\rm rms}/(\nu k_1)$, ${\rm Re_M}={\rm Pr_M Re}=u_{\rm rms}/(\eta k_1)$, and ${\rm Pe}={\rm Pr_{SGS}Re}=u_{\rm rms}/(\chi_{\rm SGS}k_1)$, where $u_{\rm rms}$ is the volume-averaged rms velocity in the CZ, $k_1=2\pi/\Delta R$ is the wavenumber corresponding to the approximate depth of the CZ with $\Delta r=0.35R$, and ${\rm Pr_M}=\nu/\eta$ and ${\rm Pr_{SGS}}=\nu/\chi_{\rm SGS}$ are the magnetic and SGS Prandtl numbers, respectively. Rotational influence on the flow is measured by the Coriolis number, ${\rm Co}=2\Omega_0/(u_{\rm rms}k_1)$. Magnetic fields are measured in terms of the equipartition field strength $B_{\rm eq}=\langle\sqrt{\mu_0\rho\boldsymbol{U}^2}\rangle$, where $\langle\,.\,\rangle$ refers to time and volume averaging over the CZ. Mean values are taken to be azimuthal averages and denoted by overbars. The Pencil Code (Pencil Code Collaboration et al. 2021)[1] was used to make the simulations.

The setup of the simulations is otherwise identical to those in Käpylä (2021) except that the amplitude of the radiative conductivity K_0 is enhanced such that in the thermodynamically saturated state, the star has a radiative core (CZ) that encompasses roughly two-thirds (one-third) of the stellar radius. Furthermore, the diffusion coefficients η, ν, and $\chi_{\rm SGS}$ have radial profiles such that their values in the radiative core are 10^2 smaller than in the CZ to avoid diffusive spreading of magnetic fields and flows into the core. This nevertheless happens in many runs during the initial transient toward a statistically steady state for the flow. This is due to the fact that the initial state of the simulations is an isentropic polytrope, and because of this choice, the star is fully convective in the early stages. To circumvent this issue, the magnetic field is rescaled to the $10^{-6}B_{\rm eq}$ level after a statistically steady state for the flow and thermodynamics is reached. The simulations are then further evolved until the magnetic field reaches a statistically steady state. Another possibility to avoid spreading the magnetic fields into the core is to add a seed magnetic field only after the hydrodynamic run has matured (e.g., Matilsky & Toomre 2021). The simulations at the higher resolutions (576^3 and 1152^3) were remeshed from such saturated snapshots from the low-resolution (288^3) cases.

3. Results

The simulations are summarized in Table 1. The models cover a modest range of Coriolis numbers between 5.6 and 17, where cyclic dynamos with a dominating axisymmetric magnetic fields are found. Runs with slower rotation produce quasi-static magnetic fields, whereas for more rapid rotation, nonaxisymmetric fields and less coherent cycles become dominant. The run with the highest resolution (Ch) has completed only one full cycle; therefore, it is not used in the statistical analysis of the cycle periods but merely to demonstrate that the cycles also persist at higher Reynolds numbers. A more comprehensive study of the simulations, including the slower and faster rotation cases, will be presented elsewhere.

3.1. Magnetic Fields and Cycles

The current simulations produce dynamos where the magnetic energy $E_{\rm mag}$ is a significant fraction of the kinetic energy $E_{\rm kin}$; see the sixth column of Table 1. The ratio $E_{\rm mag}/E_{\rm kin}$ is practically constant as a function of Co in the parameter regime studied here, which differs from the scaling found in Augustson et al. (2019), and the MAC balance, which is often assumed to hold for the saturation level of the magnetic fields (e.g., Brun & Browning 2017).

The azimuthally averaged radial magnetic fields near the surface of the star and the toroidal magnetic field near the base of the CZ for runs A, C, and D are shown in Figures 1(a)and (d), (b) and (g), (e) and (h), respectively. The rest of the runs follow very similar patterns. All of these cases show a solar-like pattern of magnetic field evolution at the surface with strong radial fields concentrated in latitudes $|\theta|<50^\circ$ and activity propagating equatorward. A weaker poleward branch is visible in some runs; see Figure 1(b). While a similar pattern

[1] https://github.com/pencil-code/

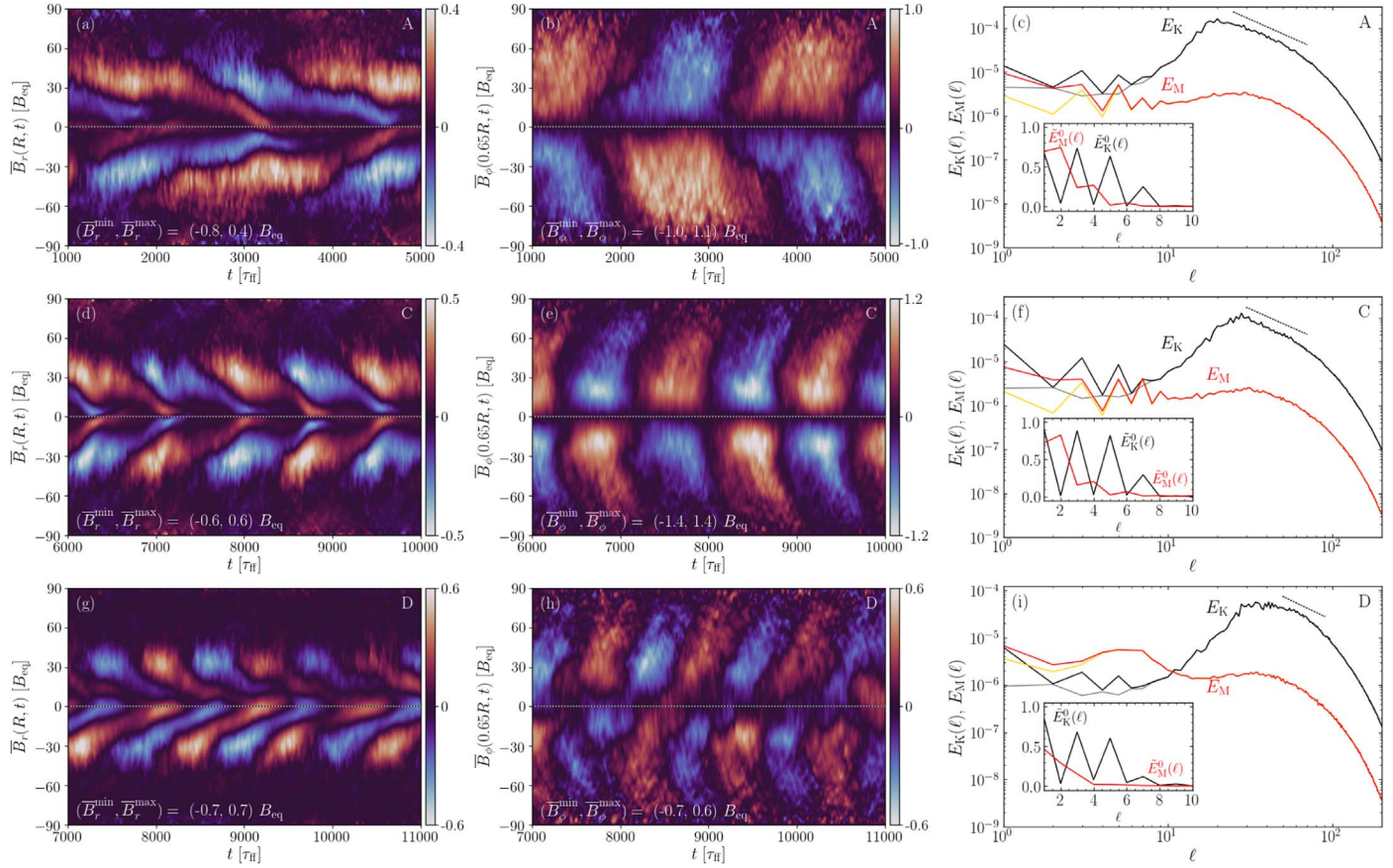

Figure 1. Panels (a), (d), and (g): azimuthally averaged radial magnetic field $\overline{B}_r(\theta, t)$ from $r = R$ for runs A (top), C (middle), and D (bottom). Panels (b), (e), and (h): azimuthally averaged toroidal field $\overline{B}_\phi(\theta, t)$ from $r = 0.65R$. The field strength is given in terms of the equipartition field B_{eq}. Panels (c), (f), and (i): power spectra of the velocity (E_K) and magnetic fields (E_M) from $r = 0.85R$ as functions of spherical harmonic degree ℓ. The gray (yellow) lines indicate nonaxisymmetric ($m \neq 0$) contributions. Dotted lines indicate the Kolmogorov $\ell^{-5/3}$ scaling. The inset shows the normalized fraction of the axisymmetric ($m = 0$) contributions.

Table 1
Summary of the Simulations

Run	Co	Re	Pe	$\mathrm{Re_M}$	$\tilde{E}_{mag}$	$\tilde{E}_{kin}^{MC}$	$\tilde{E}_{kin}^{DR}$	$\tilde{E}_{mag}^{pol}$	$\tilde{E}_{mag}^{tor}$	$P_{rot}/P_{cyc}^{surf}\,[10^{-3}]$	$P_{rot}/P_{cyc}^{deep}\,[10^{-3}]$	Grid
A	5.6	55	11	27	0.61	0.011	0.038	0.091	0.128	3.7 ± 0.8	3.4 ± 0.5	288^3
B	7.0	53	10	26	0.63	0.010	0.050	0.094	0.152	5.5 ± 0.4	5.1 ± 0.3	288^3
C	10.0	49	9	24	0.61	0.008	0.050	0.096	0.146	4.6 ± 0.4	4.1 ± 0.2	288^3
Cd	9.9	49	9	24	0.55	0.007	0.047	0.084	0.128	3.9 ± 0.6	3.9 ± 0.4	288^3
Ce	10.3	48	9	24	0.89	0.008	0.049	0.117	0.127	no cycle	no cycle	288^3
Cm	9.7	102	20	51	0.66	0.008	0.034	0.055	0.081	5.1 ± 0.5	4.9 ± 0.4	576^3
C1	9.9	100	20	100	0.71	0.008	0.033	0.030	0.044	5.0 ± 0.8	5.5 ± 0.8	576^3
Ch	9.5	260	52	130	0.69	0.008	0.035	0.026	0.041	(3.6)	(3.6)	1152^3
D	17.3	42	8	21	0.63	0.006	0.019	0.117	0.071	4.8 ± 0.3	4.0 ± 0.3	288^3

Note. Here $E_{mag} = \frac{1}{2}\langle \boldsymbol{B}^2/\mu_0 \rangle$ and $E_{kin} = \frac{1}{2}\langle \rho \boldsymbol{U}^2 \rangle$ are the total magnetic and kinetic energies, and $E_{mag}^{pol} = \frac{1}{2}\langle (\overline{B}_r^2 + \overline{B}_\theta^2)/\mu_0 \rangle$, $E_{mag}^{tor} = \frac{1}{2}\langle \overline{B}_\phi^2/\mu_0 \rangle$, $E_{kin}^{MC} = \frac{1}{2}\langle \rho(\overline{U}_r^2 + \overline{U}_\theta^2) \rangle$, and $E_{kin}^{DR} = \frac{1}{2}\langle \rho \overline{U}_\phi^2 \rangle$ refer to the energies of the poloidal and toroidal magnetic fields and the meridional circulation and differential rotation, respectively, whereas tildes refer to normalization by E_{kin}. Here P_{cyc}^{surf} and P_{cyc}^{deep} are the cycle periods measured from $\overline{B}_r$ at the surface and $\overline{B}_\phi$ at the base of the CZ. In all runs, $\mathrm{Pr_M} = 0.5$ and $\mathrm{Pr_{SGS}} = 0.2$, except run C1, where $\mathrm{Pr_M} = 1$.

can be seen for $\overline{B}_\phi$ near the surface, the dynamo wave propagates poleward near the base of the CZ.

Power spectra of the velocity and magnetic fields from a spherical harmonic decomposition are shown in Figures 1(c), (f), and (i) for runs A, C, and D. The magnetic power spectrum has its maximum at the largest possible scale ($\ell = 1$) for all runs. The maximum of the velocity power occurs at $\ell \gtrsim 20$, and the peak moves to larger ℓ with increasing rotation as the convective cells become smaller. The spectra indicate a clear separation of scales between the dominant scales of convection and those of the magnetic field. The insets of Figures 1(c), (f), and (i) show the fraction of the power in the axisymmetric ($m = 0$) part for $\ell \leqslant 10$. In this range, the odd ℓ contributions dominate the velocity field. However, these contributions are still clearly subdominant in the kinetic energy, which is dominated by convective flows with $\ell \gtrsim 10$. The large-scale

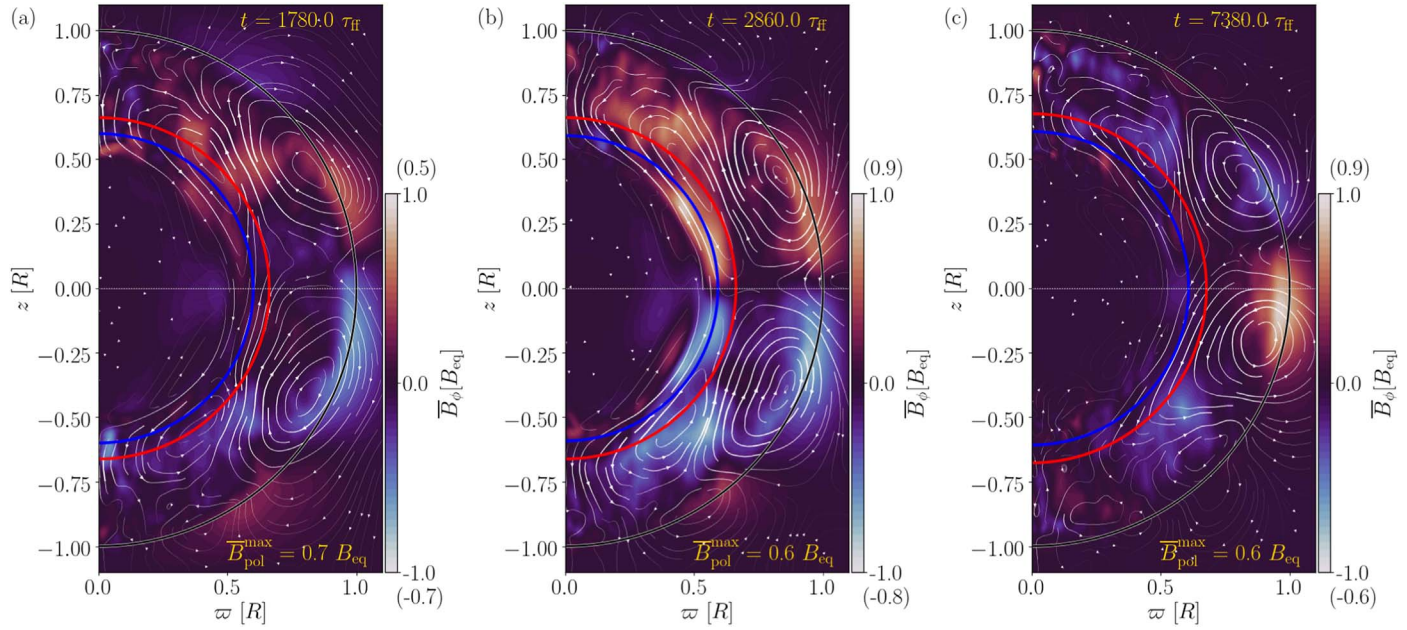

Figure 2. Azimuthally averaged magnetic fields in units of $B_{\rm eq}$ in cylindrical coordinates (ϖ, z) for runs A (a), C (b), and D (c) as functions of time for a time span of 3×10^3 freefall times corresponding to a full cycle in run A. The still shows the magnetic fields near the end of a cycle of the near-surface mode. The maximum poloidal field strength $\overline{B}_{\rm pol}^{\rm max}$ is indicated in the lower right corners. The color contours show the toroidal fields, and the arrows indicate the poloidal fields. The red, blue, and gray lines indicate the bottom of the CZ ($r_{\rm CZ}$), the bottom of the overshoot layer ($r_{\rm OZ}$), and the surface of the star ($r = R$), respectively.

(An animation of this figure is available.)

magnetic fields are dominated by the axisymmetric $(\ell, m) = (1, 0)$ component with half or more of the total power in all cases.

The evolution of the mean magnetic fields in runs A, C, and D is shown in the animations in Figure 2. These visualizations show that strong magnetic fields are concentrated near the surface of the star outside the tangent cylinder and near the interface between radiative zones and CZs inside the tangent cylinder. Strong magnetic fields can also be found within the CZ at higher latitudes. This could suggest the presence of multiple dynamo modes that have been detected in simulations previously (e.g., Beaudoin et al. 2016; Käpylä et al. 2016). In distinction to these studies, the cycles in the deep parts and near the surface in the current simulations are synchronized such that their periods are the same. Magnetic fields also penetrate into the upper part of the radiative core down to a depth $r \approx 0.5R$. To illustrate this, the bottoms of the CZ ($r_{\rm CZ}$) and the overshoot layer ($r_{\rm OZ}$) are indicated in Figure 2 by red and blue lines, respectively, where $r_{\rm CZ}$ is defined as the depth where the total convected luminosity $\langle L_{\rm conv}\rangle = \langle L_{\rm enth}\rangle + \langle L_{\rm kin}\rangle$ (see Käpylä 2021) changes from negative to positive, whereas $r_{\rm OZ}$ is where the kinetic energy luminosity $\langle L_{\rm kin}\rangle$ drops below $10^{-2} L_{\rm sim}$ (e.g., Käpylä 2019). The extent of this penetration is highly likely to be unrealistic, but such effects, albeit quantitatively different, can still conceivably occur at the interfaces of stellar radiative and convective zones.

The sensitivity of the dynamo solution was tested using two runs branched from run C in which the magnetic diffusivity was either decreased (run Cd) or enhanced (run Ce) by an order of magnitude in the exterior $r > 1.03R$. Run Cd shows only small differences from run C, whereas in run Ce, the dynamo mode switches to a nonoscillatory state. This suggests that the dynamo solution is sensitive to the boundary conditions (see also Pipin & Kosovichev 2011; Bonanno 2016). This could imply that the typically applied radial field or potential field extrapolation conditions are too restrictive.

3.2. Flow States and Dynamo Considerations

All of the current simulations are in the solar-like differential rotation regime, which is characterized by a faster equator and slower poles; see Figure 3(a). However, the differential rotation is generally weak, such that the amplitude is typically of the order of a couple of percent of Ω_0 everywhere except near the axis, where the data are poorly converged. This is also apparent from the seventh and eighth columns of Table 1, which show that the energies associated with differential rotation and meridional circulation are at most a few percent of the total kinetic energy. This is partly due to the damping of flows in the exterior, which exerts a torque that opposes differential rotation. Nevertheless, the current simulations also show a minimum of $\overline{\Omega}$ at midlatitudes, which has been conjectured to be the cause of equatorward migration by a dominating $\alpha\Omega$ dynamo in earlier spherical shell simulations (Warnecke et al. 2014).

The other ingredient in such models is the kinetic helicity, $\mathcal{H} = \overline{\boldsymbol{\omega} \cdot \boldsymbol{U}}$, where $\boldsymbol{\omega} = \boldsymbol{\nabla} \times \boldsymbol{U}$ is the vorticity, which is negative (positive) in the upper (lower) part of the CZ in the northern hemisphere (Figure 3(b)). The kinetic helicity is taken as a proxy of the mean-field α effect with $\alpha \propto -\mathcal{H}$ (e.g., Krause & Rädler 1980). A sign change of $\mathcal{H}$ occurs in the deep layers of the CZ everywhere except near the equator, which is a common feature in overshooting convection (e.g., Ossendrijver et al. 2001; Käpylä et al. 2009). Thus, the sign of kinetic helicity follows the sign of $\boldsymbol{g} \cdot \boldsymbol{\Omega}$ in the bulk of the CZ, and a significant helicity inversion and consequent reversal of the dynamo wave as suggested by Duarte et al. (2016) do not occur. In the saturated regime of the dynamo, the small-scale current helicity $\mathcal{C} = -\overline{\boldsymbol{j} \cdot \boldsymbol{b}}/\overline{\rho}$, where $\boldsymbol{b} = \boldsymbol{B} - \overline{\boldsymbol{B}}$ is the fluctuating magnetic field and $\boldsymbol{j} = \boldsymbol{\nabla} \times \boldsymbol{b}/\mu_0$, can become significant. Figure 3(c) indicates that the contribution from current helicity is of opposite sign but roughly an order of magnitude weaker than $\mathcal{H}$ and therefore subdominant in the dynamo action.

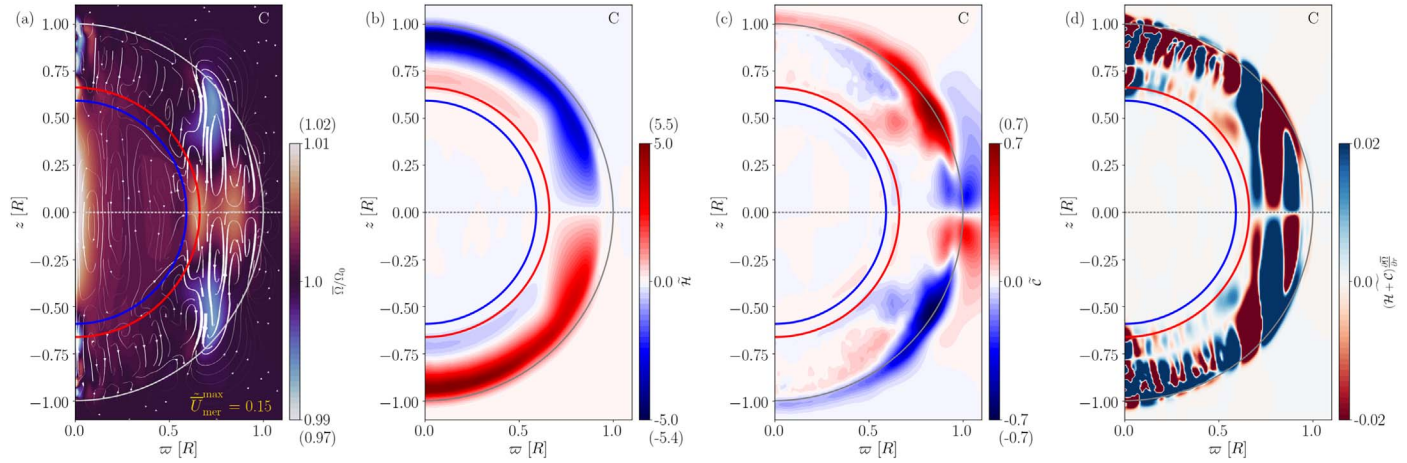

Figure 3. Normalized time-averaged mean angular velocity $\overline{\Omega}/\Omega_0 = \overline{U}_\phi/(r\sin\theta\Omega_0) + 1$ (color contours) and meridional circulation (arrows) (a), normalized kinetic helicity $\tilde{\mathcal{H}} = \mathcal{H}/(u_{\rm rms}\omega_{\rm rms})$ (b), normalized current helicity $\tilde{\mathcal{C}} = \mathcal{C}/(u_{\rm rms}\omega_{\rm rms})$ (c), and normalized product $(\mathcal{H}+\mathcal{C})\frac{\partial\overline{\Omega}}{\partial r} = \tau_{\rm ff}^3(\mathcal{H}+\mathcal{C})\frac{\partial\overline{\Omega}}{\partial r}$ (d) from run C.

The helicities are weak in the upper part of the radiative core, yet significant poloidal fields are present there; see Figure 2. Turbulent pumping of fields from the CZ down to the radiative zone and subsequent amplification by shear are a plausible scenario to explain the strong fields in the upper part of the radiative core. The weaker fields in the radiative layer in run D are likely due to roughly thrice smaller relative differential rotation in comparison to run C.

The product of the radial gradient of $\overline{\Omega}$ and $\mathcal{T} = \mathcal{H} + \mathcal{C}$ determines the propagation direction of the dynamo wave in $\alpha\Omega$ dynamos (Parker 1955; Yoshimura 1975). Figure 3(d) indicates both poleward ($\mathcal{T}\partial_r\overline{\Omega} < 0$) and equatorward ($\mathcal{T}\partial_r\overline{\Omega} > 0$) regions outside the tangent cylinder and predominantly poleward propagation in the lower part of the CZ inside the tangent cylinder. It is tempting to associate the equatorward branch near the surface with a corresponding patch of positive $\mathcal{T}\partial_r\overline{\Omega}$ and the poleward branch in the deep parts with a corresponding patch of negative $\mathcal{T}\partial_r\overline{\Omega}$ (in the northern hemisphere). However, the Parker–Yoshimura rule strictly applies only in the case of a pure $\alpha\Omega$ dynamo with spatially constant helicity and turbulent diffusion. The low ratio of toroidal to poloidal magnetic energies (10th and 9th columns in Table 1) also suggests that the dynamos in the current simulations are not of the $\alpha\Omega$ type.

In addition to the already-mentioned helicity inversion, further possibilities to excite equatorward propagation include the near-surface shear (e.g., Brandenburg 2005) and an α^2 dynamo with a sign change of helicity at the equator (e.g., Mitra et al. 2010). Neither of these possibilities can be ruled out immediately with the data at hand, although the shear near the surface is not very prominent in the current simulations. However, explanations based on such simple models should be considered with caution in light of a recent study by Warnecke et al. (2021), who found that explaining the cause and evolution of large-scale magnetism in a spherical shell simulation required a mean-field model with 18 turbulent transport coefficients derived using the test-field method (e.g., Schrinner et al. 2007).

3.3. Rotational Scaling of Dynamo Cycles and Magnetic Energy

Long-term observations of chromospheric emission of late-type stars suggest that many such stars have magnetic cycles similar to the Sun (e.g., Baliunas et al. 1995). It has also been suggested that the ratio of stellar rotation period to cycle period fall into a number branches as a function of the Coriolis number (e.g., Brandenburg et al. 1998, 2017). These studies suggest inactive and active branches with $P_{\rm rot}/P_{\rm cyc} \propto {\rm Co}^\beta$, where $\beta > 0$. However, the exact nature (Olspert et al. 2018) and the significance of the branches continue to be debated (e.g., Boro Saikia et al. 2018). It is nevertheless interesting to measure the ratio $P_{\rm rot}/P_{\rm cyc}$ from simulations to see if any systematics can be found. This has been done in a handful of studies; data from Warnecke (2018) indicate $\beta = -0.99 \pm 0.05$, whereas data from Strugarek et al. (2018) show a steeper relation with $\beta = -1.57 \pm 0.12$; see Figure 4(a). Furthermore, the results from a more heterogeneous set of simulations by Viviani et al. (2018) also suggest $\beta < 0$. A notable exception is the study of Guerrero et al. (2019), with $\beta = -0.47 \pm 0.15$ for slow and $\beta = 1.17 \pm 0.05$ for rapid rotation; see Figure 4(a).

The cycle periods from the current simulations are computed using the *libeemd* library (Luukko et al. 2015) using the ensemble empirical mode decomposition. Periods are determined from $\overline{B}_r(R, \theta_d, t)$ and $\overline{B}_\phi(0.65R, \theta_d, t)$, where $-45° < \theta_d < 45°$ is the range of latitudes considered. The mode with the largest energy is identified as the primary cycle, and the period is computed from zero crossings of that mode. The mean cycle period $P_{\rm cyc}$ is taken to be the average over θ_d. Error estimates are provided by dividing the time series into three parts and repeating the analysis for each part. The largest deviation from the mean period over the full time series is taken to represent the error. The current results indicate that the ratio $P_{\rm rot}/P_{\rm cyc}$ is almost independent of Co in the parameter range explored here with $\beta = 0.14 \pm 0.16$ ($\beta = 0.03 \pm 0.25$) for the surface (deep) cycles; see Figure 4(a). These results differ qualitatively from those of Strugarek et al. (2018) and Warnecke (2018) that are also shown in Figure 4(a).[2] Guerrero et al. (2019) reported results for $P_{\rm rot}/P_{\rm cyc}$ that are similar to those obtained here from models that also included a radiative layer below the CZ. However, the magnetic field configurations achieved in that study are quite different from those here such that, e.g., no clear equatorward migration is obtained.

[2] The Rossby numbers from Strugarek et al. (2018) and Guerrero et al. (2019) were converted to Coriolis numbers as ${\rm Co} = 2\pi/{\rm Ro}_{\rm b}$ and $2\pi/{\rm Ro}$, respectively.

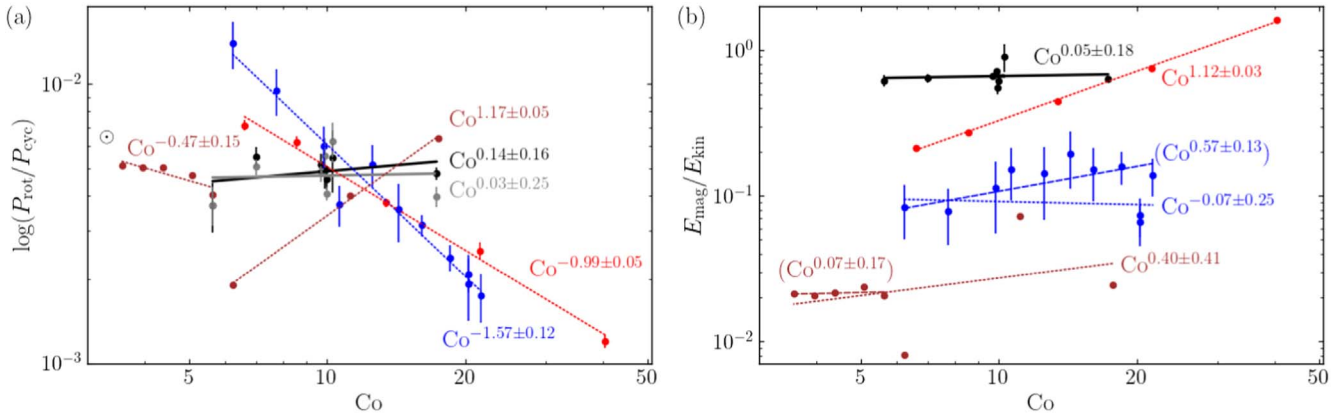

Figure 4. Ratios of rotation to cycle period as a function of Co with $P_{\rm rot}/P_{\rm cyc}^{\rm surf}$ (black) and $P_{\rm rot}/P_{\rm cyc}^{\rm deep}$ (gray). Additional data are from Warnecke (2018; red), Strugarek et al. (2018; blue), and Guerrero et al. (2019; brown). The dotted lines show power-law fits to the data (a). The solar data point ($\odot$) is computed using data from Brandenburg et al. (2017) with $\mathrm{Co} = 2\pi\tau/P_{\rm rot}$, where τ is the convective turnover time. Panel (b) shows the ratio $E_{\rm mag}/E_{\rm kin}$ as a function of Co from the same studies. Fits to full data (dotted lines) and subsets (dashed lines) where some data are omitted are shown (see text).

The ratio $P_{\rm rot}/P_{\rm cyc}$ in the current simulations is between $(3\ldots5)\times10^{-3}$, which is close to the solar value $P_{\rm rot}^{\odot}/P_{\rm cyc}^{\odot}\approx 6.5\times10^{-3}$ with $P_{\rm rot}^{\odot}=26$ days and $P_{\rm cyc}^{\odot}\approx11$ yr. This and the near independence of $P_{\rm rot}/P_{\rm cyc}$ on Co suggests that the dynamos in the current simulations might capture some of the characteristics of stars in the inactive branch, to which the Sun also belongs (e.g., Brandenburg et al. 1998). However, at the same time, it is clear that the current simulations do not reproduce many other aspects of the Sun, such as the structure and magnitude of the differential rotation.

Figure 4(b) shows the ratio of magnetic to kinetic energy for the current simulations, as well as from the simulations of Warnecke (2018),[3] Strugarek et al. (2018), and Guerrero et al. (2019). The data for $E_{\rm mag}/E_{\rm kin}$ are heterogeneous, similar to $P_{\rm rot}/P_{\rm cyc}$, although the current results and those of Guerrero et al. (2019) are consistent with independence of rotation. This is true for the full data set and for the slow rotation runs with $\mathrm{Co}<6$ in the latter study. The data from Warnecke & Käpylä (2020) and Strugarek et al. (2018) indicate a clearly increasing trend as a function of rotation if the two outliers in the latter case around $\mathrm{Co}=20$ are omitted. However, only the results of Warnecke & Käpylä (2020) are near the scaling expected from the MAC balance, which suggests $E_{\rm mag}/E_{\rm kin}\propto\mathrm{Co}$. It appears that the different behaviors of $P_{\rm rot}/P_{\rm cyc}$ and $E_{\rm mag}/E_{\rm kin}$ are connected such that a flat or increasing $P_{\rm rot}/P_{\rm cyc}$ with rotation implies a near independence of $E_{\rm mag}/E_{\rm kin}$ on Co (present study and Guerrero et al. 2019), while a decreasing $P_{\rm rot}/P_{\rm cyc}$ suggests an increasing $E_{\rm mag}/E_{\rm kin}$ (Strugarek et al. 2018; Warnecke & Käpylä 2020).

4. Conclusions

Star-in-a-box simulations of a solar-like convective envelope were shown to produce solar-like magnetic activity on a limited range of rotation rates. The current simulations share many characteristics of earlier spherical shell models (e.g., Käpylä et al. 2012), including a local minimum of $\overline{\Omega}$ at midlatitudes, which has been conjectured to be the cause of equatorward migration in those studies (Warnecke et al. 2014). However, the magnetic cycles in the current simulations show differences from the earlier studies in that the equatorward migration of the active latitudes is not restricted to midlatitudes with negative radial differential rotation. Furthermore, the rotational scaling of the cycles is qualitatively different from the earlier studies in spherical shells (e.g., Warnecke 2018), with a weak dependence of $P_{\rm rot}/P_{\rm cyc}$ on rotation.

However, several differences from earlier studies can be readily identified. These include the addition of a simplified corona, which provides a free surface for the magnetic field, rather than imposing simplified surface boundary conditions (see also Warnecke et al. 2016). Another difference is the inclusion of the radiative core, where strong magnetic fields can be stored and possibly amplified by means other than helical convection (e.g., Guerrero et al. 2019). Finally, changing the geometry and size of the system also allows, in general, a wider spectrum of dynamo modes that can be excited. A more detailed analysis of the maintenance of the magnetic fields is needed to precisely pinpoint the differences from the earlier studies. Nevertheless, the current results suggest that regions outside of the CZ shape the global dynamo solutions, and that perhaps the dynamos in the Sun and other inactive stars harbor dynamos where such effects are important.

This work was supported by Deutsche Forshungsgemeinschaft Heisenberg grant KA4825/4-1. The simulations were made using the HLRN-IV supercomputers Emmy and Lise hosted by the North German Supercomputing Alliance (HLRN) in Göttingen and Berlin, Germany. I thank Gustavo Guerrero and Jörn Warnecke for sharing data from their simulations, and the anonymous referee for constructive comments.

Software: Pencil Code (Pencil Code Collaboration et al. 2021), numpy (Harris et al. 2020).

ORCID iDs

Petri J. Käpylä https://orcid.org/0000-0001-9619-0053

References

Augustson, K. C., Brun, A. S., & Toomre, J. 2019, ApJ, 876, 83
Baliunas, S. L., Donahue, R. A., Soon, W. H., et al. 1995, ApJ, 438, 269
Beaudoin, P., Simard, C., Cossette, J.-F., & Charbonneau, P. 2016, ApJ, 826, 138
Bice, C. P., & Toomre, J. 2020, ApJ, 893, 107
Bonanno, A. 2016, ApJL, 833, L22
Boro Saikia, S., Marvin, C. J., Jeffers, S. V., et al. 2018, A&A, 616, A108

[3] Data taken from Warnecke & Käpylä (2020).

Brandenburg, A. 2005, ApJ, 625, 539
Brandenburg, A., Mathur, S., & Metcalfe, T. S. 2017, ApJ, 845, 79
Brandenburg, A., Nordlund, A., & Stein, R. F. 2000, in Geophysical and Astrophysical Convection, Contributions from a workshop sponsored by the Geophysical Turbulence Program at the National Center for Atmospheric Research,, October, 1995, Astrophysical convection and dynamos, ed. P. A. Fox & R. M. Kerr (Amsterdam: Gordon and Breach), 85
Brandenburg, A., Saar, S. H., & Turpin, C. R. 1998, ApJL, 498, L51
Brown, B. P., Miesch, M. S., Browning, M. K., Brun, A. S., & Toomre, J. 2011, ApJ, 731, 69
Brun, A. S., & Browning, M. K. 2017, LRSP., 14, 4
Cole, E., Brandenburg, A., Käpylä, P. J., & Käpylä, M. J. 2016, A&A, 593, A134
Dobler, W., Stix, M., & Brandenburg, A. 2006, ApJ, 638, 336
Duarte, L. D. V., Wicht, J., Browning, M. K., & Gastine, T. 2016, MNRAS, 456, 1708
Ghizaru, M., Charbonneau, P., & Smolarkiewicz, P. K. 2010, ApJL, 715, L133
Guerrero, G., Zaire, B., Smolarkiewicz, P. K., et al. 2019, ApJ, 880, 6
Hanasoge, S. M., Duvall, T. L., & Sreenivasan, K. R. 2012, PNAS, 109, 11928
Harris, C. R., Millman, K. J., van der Walt, S. J., et al. 2020, Natur, 585, 357
Hathaway, D. H. 2010, LRSP, 7, 1
Hotta, H., & Kusano, K. 2021, NatAs, 5, 1100
Käpylä, M. J., Käpylä, P. J., Olspert, N., et al. 2016, A&A, 589, A56
Käpylä, P. J. 2019, A&A, 631, A122
Käpylä, P. J. 2021, A&A, 651, A66
Käpylä, P. J., Käpylä, M. J., & Brandenburg, A. 2014, A&A, 570, A43
Käpylä, P. J., Korpi, M. J., & Brandenburg, A. 2009, A&A, 500, 633
Käpylä, P. J., Mantere, M. J., & Brandenburg, A. 2012, ApJL, 755, L22
Krause, F., & Rädler, K.-H. 1980, Mean-field Magnetohydrodynamics and Dynamo Theory (Oxford: Pergamon Press)
Luukko, P., Helske, J., & Räsänen, E. 2015, Comput. Stat, 31, 545
Matilsky, L. I., & Toomre, J. 2021, arXiv:2105.05412
Mitra, D., Tavakol, R., Käpylä, P. J., & Brandenburg, A. 2010, ApJL, 719, L1
Nelson, N. J., Brown, B. P., Brun, A. S., Miesch, M. S., & Toomre, J. 2013, ApJ, 762, 73
Olspert, N., Lehtinen, J. J., Käpylä, M. J., Pelt, J., & Grigorievskiy, A. 2018, A&A, 619, A6
O'Mara, B., Miesch, M. S., Featherstone, N. A., & Augustson, K. C. 2016, AdSpR, 58, 1475
Ossendrijver, M., Stix, M., & Brandenburg, A. 2001, A&A, 376, 713
Parker, E. N. 1955, ApJ, 122, 293
Pencil Code Collaboration, Brandenburg, A., Johansen, A., et al. 2021, JOSS, 6, 2807
Pipin, V. V., & Kosovichev, A. G. 2011, ApJL, 727, L45
Schrinner, M., Rädler, K.-H., Schmitt, D., Rheinhardt, M., & Christensen, U. R. 2007, GApFD, 101, 81
Schumacher, J., & Sreenivasan, K. R. 2020, RvMP, 92, 041001
Strugarek, A., Beaudoin, P., Charbonneau, P., & Brun, A. S. 2018, ApJ, 863, 35
Viviani, M., Warnecke, J., Käpylä, M. J., et al. 2018, A&A, 616, A160
Warnecke, J. 2018, A&A, 616, A72
Warnecke, J., & Käpylä, M. J. 2020, A&A, 642, A66
Warnecke, J., Käpylä, P. J., Käpylä, M. J., & Brandenburg, A. 2014, ApJL, 796, L12
Warnecke, J., Käpylä, P. J., Käpylä, M. J., & Brandenburg, A. 2016, A&A, 596, A115
Warnecke, J., Rheinhardt, M., Viviani, M., et al. 2021, ApJL, 919, L13
Yoshimura, H. 1975, ApJ, 201, 740